

Circumnuclear star formation in Mrk 42 mapped with Gemini Near-infrared Integral Field Spectrograph

Moiré G. Hennig^{1*}, Rogemar A. Riffel¹, O. L. Dors², Rogerio Riffel³,
Thaisa Storchi-Bergmann³ and Luis Colina^{4,5}

¹ Departamento de Física, CCNE, Universidade Federal de Santa Maria, 97105-900, Santa Maria, RS, Brazil

² Universidade do Vale do Paraíba, Av. Shishima Hifumi 2911, CEP 12244-000, São José dos Campos, SP, Brazil

³ Departamento de Astronomia, IF, Universidade Federal do Rio Grande do Sul, CP 15051, 91501-970, Porto Alegre, RS, Brazil

⁴ Centro de Astrobiología (CAB, CSIC-INTA), Carretera de Ajalvir, 28850 Torrejón de Ardoz, Madrid, Spain

⁵ ASTRO-UAM, Universidad Autónoma de Madrid (UAM), Unidad Asociada CSIC, Madrid, Spain

Accepted XXX. Received YYY; in original form ZZZ

ABSTRACT

We present Gemini Near-infrared Integral Field Spectrograph (NIFS) observations of the inner 1.5×1.5 kpc² of the narrow-line Seyfert 1 galaxy Mrk 42 at a spatial resolution of 60 pc and spectral resolution of 40 km s⁻¹. The emission-line flux and equivalent width maps clearly show a ring of circumnuclear star formation regions (CNSFRs) surrounding the nucleus with radius of ~ 500 pc. The spectra of some of these regions show molecular absorption features which are probably of CN, TiO or VO, indicating the presence of massive evolved stars in the thermally pulsing asymptotic giant branch (TP-AGB) phase. The gas kinematics of the ring is dominated by rotation in the plane of the galaxy, following the large scale disk geometry, while at the nucleus an additional outflowing component is detected blueshifted by 300–500 km s⁻¹, relative to the systemic velocity of the galaxy. Based on the equivalent width of Br γ we find evidences of gradients in the age of HII regions along the ring of Mrk 42, favoring the pearls on a string scenario of star formation. The broad component of Pa β emission line presents a Full Width at Half Maximum (FWHM) of ~ 1480 km s⁻¹, implying in a mass of $\sim 2.5 \times 10^6 M_{\odot}$ for the central supermassive black hole. Based on emission-line ratios we conclude that besides the active galactic nucleus, Mrk 42 presents nuclear Starburst activity.

Key words: galaxies: individual (Mrk 42) – galaxies: active – galaxies: ISM – infrared: galaxies

1 INTRODUCTION

Since the early studies by Morgan (1958) and Sérsic & Pastoriza (1967) – see also Kennicutt (1989) – that showed that there are many spiral galaxies hosting circumnuclear star formation regions (CNSFRs), much progress has been done in our knowledge about how are these regions originated. Inflows of gas from hundred of parsec scales towards the center of galaxies are now commonly observed (e.g. Riffel et al. 2008; Riffel, Storchi-Bergmann & Winge 2013; Diniz et al. 2015). These inflows, besides possibly feeding the central supermassive black hole (SMBH) can also trigger (circum-)nuclear star formation, such as it has been observed in some active galaxies. This relation between nuclear activity and star formation is commonly called

as the Active Galactic Nuclei-Starburst (AGN-Starburst) connection (Perry & Dyson 1985; Norman & Scoville 1988). Studies on AGN-Starburst connections are of fundamental importance to explain the possible co-evolution of SMBH and its host galaxy, as the star formation in the central region leads to the growth of the bulge mass, while gas accreted by the SMBH leads to the its growth (Ferrarese & Merritt 2000; Gebhardt et al. 2000).

In barred galaxies the material probably flows through the large scale bars to reach the circum-nuclear region (Sakamoto et al. 1999; Jogee et al. 2005), where it can be accumulated and forming a gas reservoir favoring the star formation in circum-nuclear rings with radius of a few hundreds of parsecs (Simões et al. 2007; Böker et al. 2008). Inflows of ionized and molecular gas within the inner kiloparsec of nearby active galaxies have also been observed in association to dust spirals using optical (e.g. Schnorr-Müller et al. 2014a,b)

* E-mail: moiregh@gmail.com

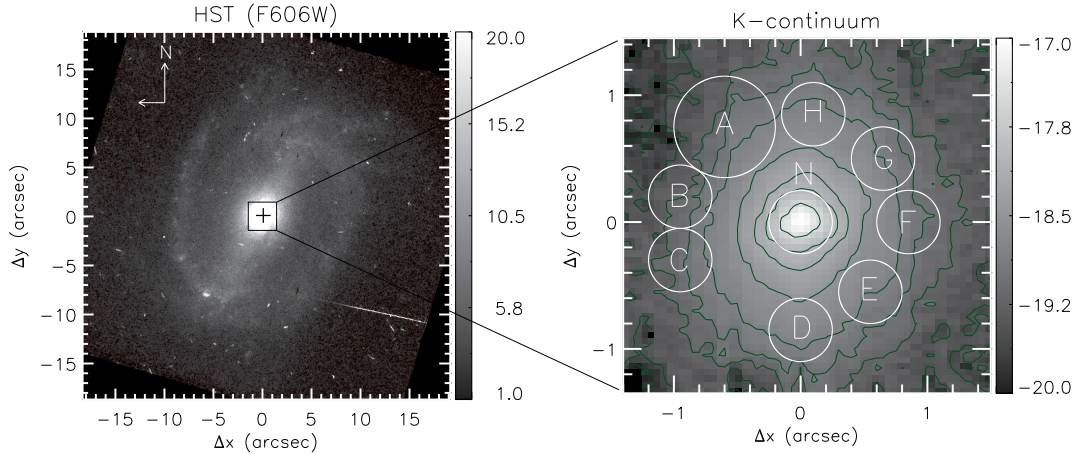


Figure 1. The left panel shows an HST image of Mrk 42 obtained through the filter F606W (Malkan et al. 1998), with the FOV of the NIFS observations indicated by the central square. The right panel shows the K-continuum image obtained from the NIFS datacube. The color bars show the fluxes in arbitrary units for the HST image and in logarithmic units of $\text{erg cm}^{-2} \text{s}^{-1} \text{\AA}^{-1}$ for the NIFS. The circles correspond to the locations where the CNSFRs are observed, as seen in the Equivalent Width map for the Pa β emission line in Figure 4.

and near-infrared (hereafter near-IR, e.g. Riffel et al. 2008; Riffel, Storchi-Bergmann & Winge 2013) Integral Field Spectroscopy (IFS). Rings of circumnuclear star-formation regions (CNSFRs) are commonly observed in spiral galaxies, being associated to the inner and outer Lindblad resonances and can be produced by bar or oval distortion perturbations (e.g. Schwarz 1981). Such rings are more frequently found in AGN hosts in comparison to normal galaxies or starbursts (Hunt & Malkan 1999; Hunt et al. 1999). In addition, Low-Ionization Nuclear Emission-line Regions (LINERs) hosts show higher fractions of inner rings, while for Seyfert galaxies outer rings are more often observed, with ring fractions being several times larger than in normal galaxies (Hunt & Malkan 1999). Regarding the presence of bars, Hunt & Malkan (1999) found that active and non-active galaxies show similar incidence of them, thus the distinct fraction of rings seems to be the only morphological difference between active and non-active galaxies.

Several recent studies were aimed in constraining the physical properties of CNSFRs in active and non-active galaxies (Davies et al. 2007; Dors et al. 2008; Böker et al. 2008; Falcón-Barroso et al. 2014; van der Laan et al. 2015; Riffel et al. 2016). CNSFRs show star-formation rates of 10^{-3} – $10^{-1} M_{\odot} \text{ yr}^{-1}$ and have ionized gas masses ranging from 10^4 to $10^5 M_{\odot}$ (e.g. Dors et al. 2008; Riffel et al. 2016). The scenario that leads to the formation of CNFRs is still an open issue and the way the material settles in the circumnuclear region may represent different processes for the star formation. For example, Knapen (2005) considers a distinction between CNSFRs and nuclear star formation regions: in the former, the material that arrives in the central region forms a circum-nuclear ring with ~ 2 kpc radius, while in the latter the material settles in more internal regions (within a few hundred parsecs). Two main scenarios have been proposed for the origin of CNSFRs: the *popcorn* and *pearls on a string* scenarios (Böker et al. 2008; Elmegreen 1994). In the first scenario, after an increase in the gas density due to accumulation of material in the ring, the stellar clusters are formed at random positions. In this scenario, there are no age sequence for the star clusters along the ring. In the sec-

ond scenario, the gas flows to the central region along bars and is accumulated at two locations (at the tips of the bar), originating over-dense regions - ODR, in which the stars are formed. Due to the differential rotation of the bar and the disk of the galaxy, the star formation “moves” along the ring, leading to a sequence of ages for young stellar clusters.

Until now, studies on star formation in CNSFRs seem to have not produced yet conclusive results about the star formation scenario. In fact, Mazzuca et al. (2008), who used photometric H α data of 22 CNSFRs, found that about half of the rings contain azimuthal age gradients, while Dors et al. (2008) and Riffel et al. (2016) did not find any sequence of age in CNSFRs located in three galaxies, using optical and near-IR IFS.

With the goal to improve the knowledge of star formation in CNSFRs, increasing the sample of objects, we have used near-IR IFS to study the circumnuclear star formation and nuclear activity in the nearby active galaxy Mrk 42. This object is classified as an SBa galaxy harboring a Narrow-Line Seyfert 1 nucleus (Malkan et al. 1998), being located at a redshift $z = 0.024634$ (Falco et al. 1999), corresponding to a distance of 102.6 Mpc by assuming a Hubble constant $H_0 = 72 \text{ km s}^{-1} \text{ Mpc}^{-1}$. At this distance, $1''$ corresponds to 497 pc at the galaxy. It harbors a SMBH of mass $(0.7\text{--}1.8) \times 10^6 M_{\odot}$ as derived from scaling relations and based on the X-ray excess variance (Wang & Lu 2001; Bian & Zhao 2003; Nikolajuk, Czerny & Gryniewicz 2009).

Muñoz Marín et al. (2007) present an atlas of the central regions of 75 Seyfert galaxies imaged in the near-UV with the Hubble Space telescope (HST), including Mrk 42 in their sample. They found that Mrk 42 has a very bright compact nucleus with a ring of star formation ≈ 300 pc of radius, with many stellar clusters individually resolved. Indeed, the observed spiral arm seen in Mrk 42 is very coiled, being described by Storchi-Bergmann (2008) as clear ring of star-formation surrounding the nucleus. The size of the ring of CNSFRs observed in Mrk 42 is similar to that derived for the rings in other galaxies, such as NGC 1068 and NGC 7469, resulting from a gas ring formed through bar-forcing at the inner Lindblad resonance (e.g. Wilson et al.

1991). A broad band HST image of Mrk 42 obtained with the Wide Field Planetary Camera 2 (WFPC2) through the filter F606W shows grand-design nuclear spiral arms, originating from a bar with an extent of $15''$ oriented along position angle $PA = -20/160^\circ$, and the CNSFRs ring is clearly observed (Malkan et al. 1998; Deo, Crenshaw & Kraemer 2006). The nuclear region of Mrk 42 presents strong $6.2 \mu\text{m}$ PAH emission as revealed by Spitzer mid-infrared spectroscopy, with a luminosity of $2 \times 10^{41} \text{ erg s}^{-1}$, providing strong evidence for intense ongoing star formation in the circumnuclear region (Sani et al. 2010).

We use J, H and K-band IFS of the inner $3'' \times 3''$ ($1.5 \times 1.5 \text{ kpc}^2$) of Mrk 42 to map, for the first time, its near-IR emission-line flux distributions and kinematics. This paper is organized as follows. In section 2, we describe the observations and data reduction procedures. In section 3 we present maps for the fluxes, flux ratios, line-of-sight velocities and velocity dispersions of the molecular and ionized gas emission lines. These maps are discussed in section 4 and our conclusions are presented in section 5.

2 OBSERVATIONS AND DATA REDUCTION

The observations of Mrk 42 were done using the Gemini Near-infrared Integral Field Spectrograph (NIFS, McGregor et al. 2003) operating with the ALTAIR adaptive optics module on the Gemini North telescope in May 2014 under the programme GN-2014A-Q-28. The J, H and K-band observations were obtained following the standard Object-Sky-Object dithering sequence, with individual exposures of 520 sec each. We obtained eight on-source exposures for each band, and thus the total integration time is ~ 1.2 hours per band. The NIFS has a square field of view of $3'' \times 3''$, which was centred at the nucleus of the galaxy during the observations.

For the J-band, we used the filter J_G5603, resulting in a spectral range from $1.15 \mu\text{m}$ to $1.35 \mu\text{m}$ and a spectral resolution of $\approx 1.7 \text{ \AA}$, as obtained from the Full Width at Half Maximum (FWHM) of typical Ar calibration lamp lines. The H-band observations were centred at $1.65 \mu\text{m}$, covering a spectral range between $1.48 \mu\text{m}$ and $1.80 \mu\text{m}$ at a spectral resolution of $\approx 2.5 \text{ \AA}$ using H_G5604 filter. In K-band the resulted spectral range is $2.01\text{--}2.42 \mu\text{m}$, centred at $2.20 \mu\text{m}$ and the observations were performed using the K_G5605 filter. The resulting spectral resolution for the K-band is $\approx 3.2 \text{ \AA}$, as obtained from FWHM of typical ArXe wavelength calibration lamp emission lines.

The data reduction followed the standard procedure of near-IR spectroscopic data treatment and was accomplished using tasks contained in the GEMINI.NIFS IRAF¹ package as well as generic IRAF tasks. The data reduction procedure included trimming of the images, flat-field correction, sky subtraction, wavelength calibration and s-distortion correction. The telluric absorptions were removed by dividing the spectra of the galaxy by the normalized spectrum of a telluric standard star of A spectral type, observed just before

or after the observations of the galaxy. These standards have also been used to flux calibrate the spectra by interpolating a blackbody function to fit the spectrum of each standard star.

Finally, individual datacubes for each exposure were created with a spaxel size of $0''.05 \times 0''.05$, which were then combined to a single datacube for each band using the *gemcombine* task of the GEMINI IRAF package. The final datacube for each band contains about 3600 spectra and covers the inner $3'' \times 3''$ of the galaxy. The angular resolution is about $0''.12$ for all bands, as obtained from the FWHM of the flux distribution of the telluric standard stars, corresponding to $\approx 60 \text{ pc}$ at the galaxy. Similar FWHM values are obtained from the flux distributions of the Pa β , Br γ and O λ 1.129 μm broad components.

In order to eliminate high frequency noise from the data, but with no loss in the image quality and preserving the flux, we used the IDL script *bandpass_filter.pro* to apply a filter of order 3 and a cutoff frequency of 0.35 Ny on all bands. The filter was chosen by comparing the filtered and original continuum image, making sure that there was no removal of intrinsic emission from the galaxy. Similar procedures were already applied to NGC 4303 SINFONI datacubes by our group (Riffel et al. 2016) and Butterworth filtering has extensively been used in the treatment of optical IFS of nearby galaxies (e.g. Ricci, Steiner & Menezes 2014; May et al. 2016).

3 RESULTS

In the left panel of Figure 1, we present an optical image of the inner $40'' \times 40''$ of Mrk 42 obtained with the HST WFPC2 through the filter F606W (Malkan et al. 1998). The central cross marks the position of the nucleus indicated by ‘+’ and the central square indicates the field of view (FOV) of the NIFS observations of $3'' \times 3''$. The nuclear grand-design spiral arms and bar are clearly seen in this image, as discussed in Deo, Crenshaw & Kraemer (2006). The right panel of this figure shows the continuum image of the nuclear region obtained from the NIFS data cube by averaging the fluxes between 2.26 and $2.28 \mu\text{m}$, a region with no strong emission/absorption lines. Although the continuum is more elongated in the direction of the bar, the presence of the bar in the inner $3'' \times 3''$ region is not evident. In addition, the K-band continuum image does not show any enhancement at the locations where the CNSFRs were detected in UV continuum images (Muñoz Marín et al. 2007), which is an expected result, since young SP are enhanced in the UV spectral region while in the near-IR just a very small fraction of their light is detected (Riffel et al. 2011). The locations of the CNSFRs are identified from the Pa β Equivalent Width map shown in the bottom-left panel of Fig. 4.

In Fig. 2 we show the J (left panel), H (center panel) and K-band (right panel) spectra for the nucleus and for the CNSFRs. These spectra were extracted within a circular aperture of $0''.25$ radius, centred at the nucleus and location of each CNSFR, identified as the locations of peak in the Equivalent Width (EqW) map for the Pa β emission line, shown in the bottom-left panel of Fig. 4. The nucleus is labeled as ‘N’ and the CNSFRs from ‘A’ to ‘H’ in Fig. 4. The size of the aperture was chosen to include most of the emis-

¹ IRAF is distributed by National Optical Astronomy Observatories, which are operated by the Association of Universities for Research in Astronomy, Inc., under cooperative agreement with the National Science Foundation

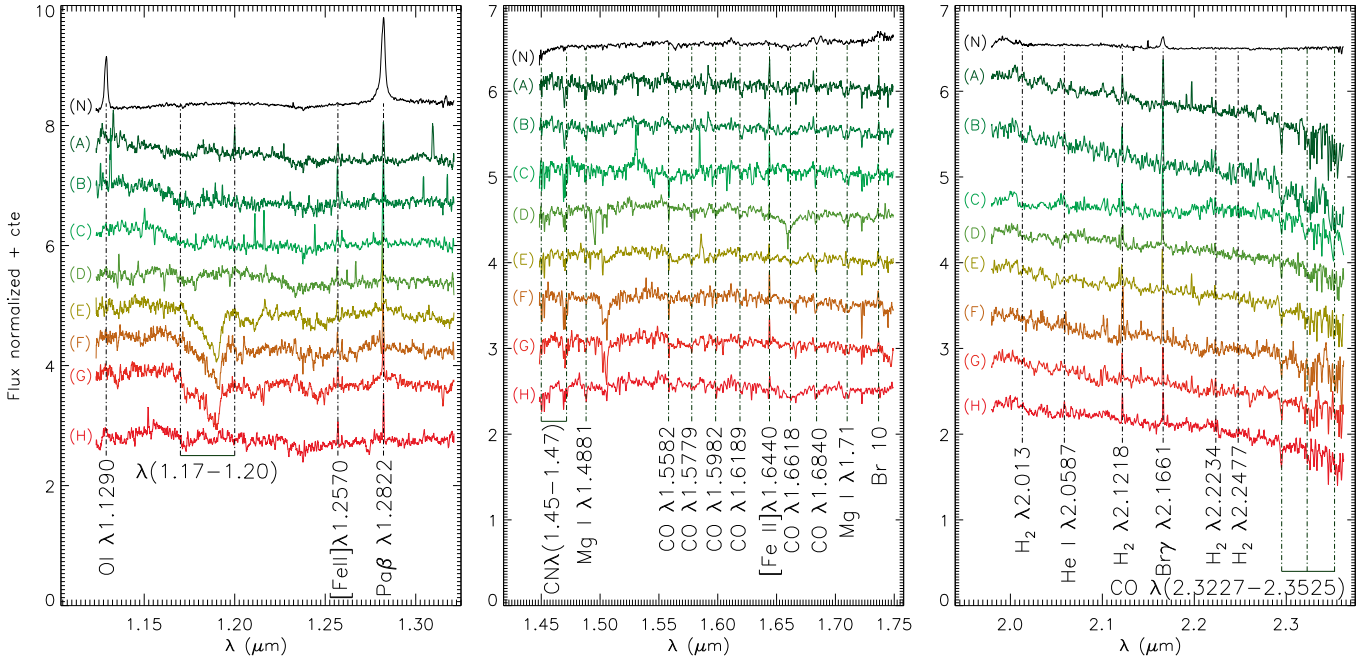


Figure 2. J (left), H (center) and K-band (right) spectra for the nucleus (top spectra) and CNSFRs. The spectra were extracted for an aperture of $0''.25$ radius centred at the locations identified by the circles in the bottom-left panel of Fig. 4 and are corrected for the Doppler shift. The exception is the location A, for which an aperture of $0''.4$ radius was used. The strongest emission and absorption lines are identified for each band.

sion from each CNSFR and for region ‘A’, a larger aperture with $0''.4$ radius was used. The spectra show several emission lines, as $[\text{Fe II}]\lambda 1.25\mu\text{m}$, $[\text{Fe II}]\lambda 1.64\mu\text{m}$, $\text{Pa}\beta$, $\text{Br}\gamma$ and $\text{H}_2\lambda 2.12\mu\text{m}$, as well as absorption features, as the CO band heads at the K and H bands. These spectral features can be used to investigate the origin and kinematics of the emitting gas, as well as physical properties of the stellar populations.

We fitted the profiles of the strongest emission lines by Gaussian curves in order to map their flux distributions and the gas kinematics. The fitting was done using the PROFIT (line-PROFILE FITting) routine (Riffel 2010). At most locations the emission line profiles of $\text{H}_2\lambda 2.12\mu\text{m}$ $[\text{Fe II}]\lambda 1.25\mu\text{m}$, $[\text{Fe II}]\lambda 1.64\mu\text{m}$, $\text{Pa}\beta$ and $\text{Br}\gamma$ are well reproduced by a single Gaussian function, but for the inner $0''.45$ radius the recombination lines were fitted with a narrow and a broad component, corresponding to an origin in the Narrow-Line Region (NLR) and Broad-Line Region (BLR), respectively. As the BLR is unresolved, the central wavelength and the width of the broad component were kept fixed at the values obtained by fitting the nuclear profiles shown in Fig. 2, while the amplitude of the Gaussian was allowed to vary. The line-of-sight velocity (V_{LOS}) of the broad component is blueshifted by 190 km s^{-1} relative to the systemic velocity of the galaxy (as derived in section 4.3) and its FWHM is 1480 km s^{-1} , which is larger than the values reported for $\text{H}\beta$ of $670\text{--}865 \text{ km s}^{-1}$ by Bian & Zhao (2003) and Wang & Lu (2001). Examples of fits for the $\text{Pa}\beta$ and $\text{H}_2\lambda 2.12\mu\text{m}$ profiles are shown in Fig. 3 for the nuclear position (top) and for the position of the CNSFR labeled as ‘A’ in Fig. 4. We used the resulting measurements for the emission-line fluxes, V_{LOS} and velocity dispersion (σ) to construct the two-dimensional maps that are presented in the following sections.

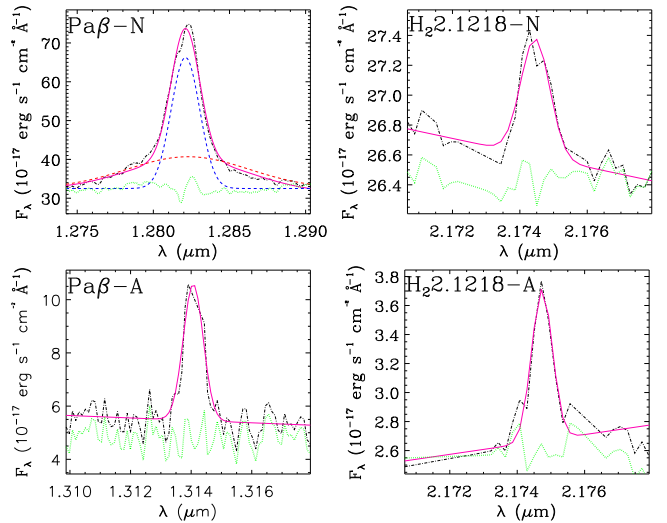


Figure 3. Examples of fits of the emission-line profiles of $\text{Pa}\beta$ (left) and $\text{H}_2\lambda 2.12\mu\text{m}$ (right) for the nucleus (top) and region A (bottom), within the apertures identified at the right panel of Fig. 1. The observed profiles are shown in black, the best fit in magenta and the residuals (plus an arbitrary constant) in green. The $\text{Pa}\beta$ profile at the nucleus was fitted by two Gaussian components: the broad component is shown as a red dashed line the narrow component as a blue dashed line.

3.1 Emission-line flux distributions and Equivalent Width maps

In the top panels of Fig. 4 we present maps for the $\text{Pa}\beta$ (left), $[\text{Fe II}]\lambda 1.64\mu\text{m}$ (center) and $\text{H}_2\lambda 2.12\mu\text{m}$ (right) emission line flux distributions. We do not show maps for $[\text{Fe II}]\lambda 1.25\mu\text{m}$ and $\text{Br}\gamma$ as they are very similar to those of $[\text{Fe II}]\lambda 1.64\mu\text{m}$

Table 1. Measured emission line fluxes in units of 10^{-18} erg cm $^{-2}$ s $^{-1}$ and the E(B-V) values for the positions labeled in Fig. 4, within a circular aperture with radius showed in the second column.

Region	R	Fluxes					E(B-V) [Pa β /Br γ]
		[Fe II] λ 1.25	Pa β	[Fe II] λ 1.64	H $_2$ λ 2.12	Br γ	
N	0''25	105.7 \pm 59.2	6 420.0 \pm 190.0	51.4 \pm 25.1	112.7 \pm 20.0	1 130.0 \pm 85.0	0.06 \pm 0.21
A	0''40	157.2 \pm 50.1	860.0 \pm 36.8	176.6 \pm 43.5	73.8 \pm 15.8	191.4 \pm 29.3	0.54 \pm 0.36
B	0''25	123.1 \pm 10.1	258.7 \pm 21.0	50.1 \pm 12.7	40.5 \pm 9.7	66.0 \pm 10.7	0.82 \pm 0.41
C	0''25	46.8 \pm 18.5	259.3 \pm 12.9	75.0 \pm 18.4	40.5 \pm 9.1	65.7 \pm 10.4	0.81 \pm 0.37
D	0''25	59.3 \pm 22.5	266.2 \pm 14.6	51.6 \pm 15.3	39.5 \pm 8.1	67.4 \pm 12.7	0.81 \pm 0.45
E	0''25	84.5 \pm 26.4	308.7 \pm 15.2	63.8 \pm 16.1	30.8 \pm 6.3	73.3 \pm 8.3	0.68 \pm 0.27
F	0''25	54.8 \pm 13.4	268.0 \pm 16.7	77.7 \pm 14.0	66.1 \pm 13.5	69.3 \pm 8.4	0.85 \pm 0.30
G	0''25	60.1 \pm 23.9	282.3 \pm 18.1	83.7 \pm 18.9	44.2 \pm 7.3	61.3 \pm 7.9	0.49 \pm 0.32
H	0''25	79.1 \pm 33.8	193.9 \pm 13.8	50.8 \pm 14.4	50.8 \pm 7.1	56.9 \pm 11.3	1.11 \pm 0.49

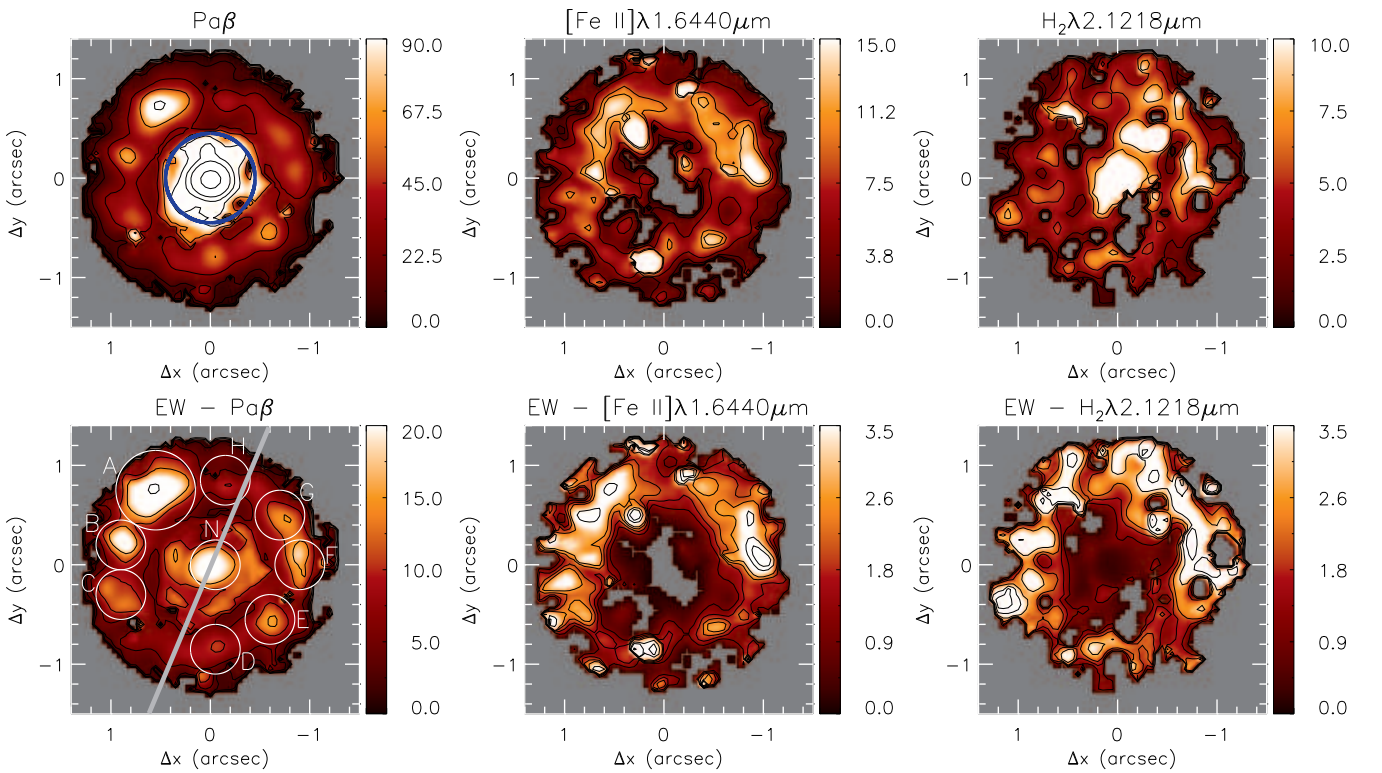


Figure 4. Top: Emission-line flux distributions for the Pa β (left), [Fe II] λ 1.64 μ m and H $_2$ λ 2.12 μ m. The color bars show the fluxes in units of 10^{-19} erg cm $^{-2}$ s $^{-1}$. For Pa β emission line, the blue circle around the nucleus delineates the region (0''45 radius) where the Pa β profile was fitted by two Gaussian curves. Bottom: Equivalent width maps for Pa β , [Fe II] λ 1.25 μ m and H $_2$ λ 2.12 μ m emission-lines. The color bars show the EqW in Å. The circles shown in the Pa β EW map correspond to the locations of the CNSFRs and the gray line marks the orientation of the bar, as seen from the HST image of Fig. 1.

and Pa β , respectively, but noisier. The gray regions in the flux maps represent masked locations where the uncertainties in flux measurements are larger than 40% or due to the non detection of the emission line. The blue circle overlaid to the Pa β flux map delineates the region where two-gaussian components were fitted to the Pa β line profile at the nuclear region. All maps clearly show the presence of the ring of CNSFRs with radius of 0''6 (\sim 300 pc), co-spatial with the ring seen in the UV HST image (Muñoz Marín et al. 2007), but some differences are seen among the maps. While strongest extra-nuclear Pa β emission is observed for region ‘A’ at the north-east of the nucleus, the H $_2$ and [Fe II] emis-

sion show stronger emission from regions located at the north-west of the nucleus. In addition, Pa β show strong nuclear emission, while a weaker nuclear emission is observed in H $_2$ and [Fe II] is not detected at the nucleus of Mrk 42. In Table 1 we present flux measurements for the [Fe II] λ 1.25 μ m, Pa β , [Fe II] λ 1.64 μ m, H $_2$ λ 2.12 μ m and Br γ emission lines for the nucleus and the CNSFRs integrated within a circular aperture of 0''25 radius, except for region ‘A’, for which an aperture of 0''4 was used.

The bottom panels of Fig. 4 show the Equivalent Width (EqW) maps for the Pa β (left), [Fe II] λ 1.64 μ m (center) and H $_2$ λ 2.12 μ m (right), which can be used to better identify the

CNSFRs, as the EqW measures the flux relative to the continuum emission and thus is ‘a pure’ line emission diagnostic. The white circles overlaid to the Pa β map (that clearly delineates the CNSFRs ring) marks the locations of the CNSFRs labeled from ‘A’ to ‘H’, as well as the position of the nucleus (‘N’). The size of the aperture was chosen to be larger than our spatial resolution bin and includes most of the line emission from the CNSFRs. The gray continuous line represents the orientation of the bar seen in the optical HST image, shown in Fig. 1. The [Fe II] λ 1.64 μ m and H₂ λ 2.12 μ m show EqW values ranging from nearly zero to ~ 5 , while Pa β shows higher values of up to 14. The highest values of Pa β EqW are seen for regions ‘A’ and ‘B’ to the north-east of the nucleus, while the other lines show the highest values both to the north-east and north-west of the nucleus. In addition, the smallest values of EqW for the H₂ are seen at the nucleus, which may be due to an increase of the continuum emission due to hot dust, as suggested by the nuclear spectrum (see Fig. 2), which is redder than the extra-nuclear spectra.

It should be noticed that the EqW values observed for all emission lines are small and a possible explanation for this is that the continuum contains an important contribution from bulge stars, that dominates the near-IR continuum emission at the central region of galaxies. In order to evaluate the contribution of the stellar bulge continuum, we followed the methodology of Dors et al. (2008) and performed aperture photometry on the continuum images to measure the continuum emission at the locations of the CNSFRs and in the surrounding regions. We concluded that the bulge contributes with about 80, 85 and 90% of the total flux in the K, H and J bands respectively. This translates to an increase in EqW values – after subtracting the contribution from the continuum – by a factor of 4 for Br γ and H₂ λ 2.12 μ m lines, a factor 6.7 for the [Fe II] λ 1.64 μ m and a factor of 10 for the Pa β and [Fe II] λ 1.25 μ m lines. The EqW values of Pa β and Br γ emission lines can be even larger if stars formed in previous episodes of star formation in the ring are present, but evaluating the contribution of these stars requires high signal-to-noise spectra to allow a proper spectral synthesis and this is beyond the scope of this paper.

3.2 Emission-line ratios

The excitation mechanisms of the [Fe II] and H₂ emission lines can be investigated using the [Fe II] λ 1.25 μ m/Pa β and H₂/Br γ line ratios, respectively (Larkin et al. 1998; Reunanen, Kotilainen & Prieto 2002; Rodríguez-Ardila et al. 2004; Rodríguez-Ardila, Riffel & Pastoriza 2005; Riffel et al. 2013; Colina et al. 2015; Lamperti et al. 2017). We show maps of these line ratios for Mrk 42 in Fig. 5. The left panel shows the [Fe II] λ 1.25 μ m/Pa β ratio map, while the H₂/Br γ map is shown in the middle panel. Gray regions represent masked locations where the signal-to-noise ratio of one or both lines was not high enough to allow good fits. In addition, we do not show the values for the inner 0 $''$ 45, for which no [Fe II] λ 1.25 μ m emission is detected (see Fig. 4) and the H₂ and Br γ are marginally detected and thus the

uncertainty in the H₂/Br γ is high. In addition, the origin of the nuclear emission will be discussed in section 3.2.

Both [Fe II] λ 1.25 μ m/Pa β and H₂ λ 2.12 μ m/Br γ flux ratio maps show values smaller than 0.6 at most locations, suggesting that the H₂ and [Fe II] lines are excited by the star-forming regions (e.g. Riffel et al. 2013). However, some differences are found between these maps. While [Fe II] λ 1.25 μ m/Pa β shows low values along the whole ring of CNSFRs, the H₂ λ 2.12 μ m/Br γ shows higher values (of up to 0.7) for the CNSFRs located to the north-west of the nucleus. In Table 2 we present the [Fe II] λ 1.25 μ m/Pa β and H₂ λ 2.12 μ m/Br γ line ratio values for the CNSFRs of Mrk 42, obtained by measuring the fluxes of the emission line from the integrated spectra shown in Fig. 2, and identified in Fig. 4. Small values of [Fe II] λ 1.25 μ m/Pa β (< 0.5) and H₂ λ 2.12 μ m/Br γ (< 1.0) are observed for all CNSFRs.

The Pa β /Br γ flux ratio can be used to map the gas extinction. The reddening ($E(B - V)$) can be obtained by

$$E(B - V) = 4.74 \log \left(\frac{5.86}{F_{\text{Pa}\beta}/F_{\text{Br}\gamma}} \right), \quad (1)$$

where $F_{\text{Pa}\beta}$ and $F_{\text{Br}\gamma}$ are the fluxes of Pa β and Br γ emission lines, respectively. We adopted the intrinsic ratio $F_{\text{Pa}\beta}/F_{\text{Br}\gamma} = 5.86$ corresponding to case B recombination for an electron temperature $T_e = 10^4$ K and electron density $N_e = 100 \text{ cm}^{-3}$ (Osterbrock & Ferland 2006) and used the extinction law of Cardelli, Clayton & Mathis (1989). The resulting $E(B - V)$ map is shown in the right panel of Fig. 5, where values ranging from 0 to 1.2 are derived. The last column of Tab. 1 shows the resulting $E(B - V)$ for the nucleus and for each CNSFR. The reddening derived for the CNSFRs of Mrk 42 are consistent with those obtained for star forming regions in other galaxies and H II galaxies (Kotilainen et al. 2000; Martins et al. 2013a; Riffel et al. 2016).

3.3 Gas velocity fields and velocity dispersion maps

Gas velocity fields (top panels) and velocity dispersion (bottom panels) maps are shown in Fig. 7. Gray regions in the maps correspond to masked locations, using the same criteria as for the emission-line flux maps (see sect. 3). The velocity fields for Pa β (top-left panel), [Fe II] (top-center panel) and H₂ (top-right panel) are presented after the subtraction of the systemic velocity of the galaxy ($V_s = 7390 \text{ km s}^{-1}$), as derived by the modeling of the Pa β velocity field by a rotating disk (see Sec. 4.3). At the inner 0 $''$ 45, where the Pa β profile was fitted by two Gaussian curves, we use the results for the narrow component. The velocity fields for all lines are similar and suggest gas rotation in the plane of the galaxy with the line of nodes oriented approximately along the north-south direction and a line-of-sight velocity (V_{LOS}) amplitude of 150 km s^{-1} . Besides ordered rotation, in the inner 0 $''$ 45 an additional velocity component is observed as indicated by the larger redshifts seen in Pa β and H₂ V_{LOS} maps, possibly due to outflows from the nucleus.

The bottom panels of Fig. 7 show the velocity dispersion maps for the Pa β (left panel), [Fe II] (center panel) and H₂ (right panel) emitting gas. These maps were corrected

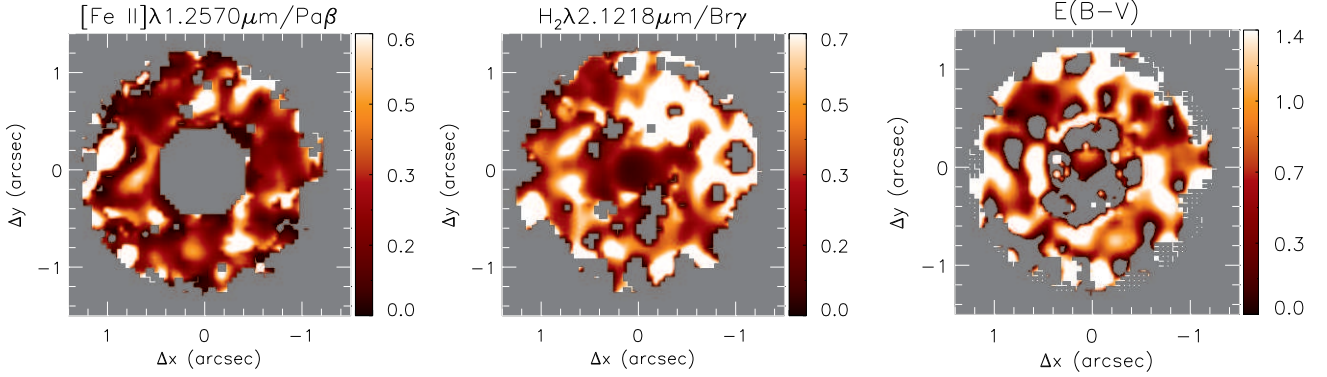


Figure 5. [Fe II] λ 1.25 μm /Pa β (left panel), H₂ λ 2.12 μm /Br γ (middle panel) emission line ratio maps and reddening map obtained from the Pa β /Br γ ratio (right panel). The gray regions represent locations where one or both lines do not present good flux measurements.

Table 2. Line-ratios, velocity dispersion and Equivalent Widths for the CNSFRs, as obtained from the integrated spectra of Fig. 2. The values for the velocity dispersion were corrected for the instrumental broadening.

P	Ratios		Velocity dispersion			Equivalent Widths			
	[Fe II]1.25/Pa β	H ₂ 2.12/Br γ	Pa β (kms ⁻¹)	[Fe II]1.64 (kms ⁻¹)	H ₂ 2.12 (kms ⁻¹)	Pa β (Å)	[Fe II]1.64 (Å)	H ₂ 2.12 (Å)	Br γ (Å)
A	0.18±0.06	0.38±0.10	25.0±1.3	53.5±15.0	35.8±9.2	14.8±3.2	2.9±0.8	2.7±0.6	7.4±1.2
B	0.47±0.05	0.61±0.18	29.8±2.8	36.4±11.3	40.5±11.3	11.4±4.1	2.4±0.7	3.8±1.1	6.6±1.7
C	0.18±0.07	0.62±0.17	26.8±1.7	50.5±14.4	40.5±10.6	10.0±2.7	3.0±0.8	3.8±1.0	6.6±1.7
D	0.22±0.08	0.59±0.16	21.4±1.7	35.3±13.0	35.2±8.9	6.8±1.8	1.2±0.4	2.2±0.5	3.6±0.7
E	0.27±0.09	0.42±0.10	22.5±1.5	36.1±11.3	22.2±6.6	8.8±3.8	1.7±0.5	2.0±0.5	4.9±0.8
F	0.20±0.05	0.95±0.23	31.4±2.3	36.3±8.2	53.5±11.9	10.9±4.5	2.8±0.7	5.6±1.4	5.8±0.9
G	0.21±0.09	0.72±0.15	29.7±2.3	40.5±11.1	25.8±5.8	9.3±2.5	2.6±0.7	3.0±0.6	4.3±0.8
H	0.41±0.18	0.89±0.22	26.8±2.5	34.3±12.2	37.0±6.2	5.8±2.0	1.4±0.4	3.1±0.5	3.5±0.8

for the instrumental broadening, as $\sigma = \sqrt{\sigma_{obs}^2 - \sigma_{inst}^2}$, where σ_{obs} is the observed velocity dispersion and σ_{inst} is the instrumental velocity dispersion given by $\sigma_{inst} = \text{FWHM}/2.355$ with the FWHM measured from typical lines present on the wavelength calibration lamp (as presented in Sec. 2). Small values of σ ($< 50 \text{ km s}^{-1}$) are observed along the ring of CNSFRs for all emission lines, while higher values are seen within the inner 0".45 for the Pa β emission with σ values of up to 200 km s^{-1} . For illustration purpose, the σ map for Pa β shows only values smaller than 80 km s^{-1} , which allows the comparison with the H₂ and [Fe II] σ maps. The high σ values seen at the nuclear region for Pa β support the interpretation that an outflow is present within the inner 0".5. Some higher σ values are also seen for the H₂ at the nucleus, reaching values of up to 80 km s^{-1} .

In Table 2 we present the velocity dispersion values obtained for each CNSFR by fitting the line profiles seen in the integrated spectra of Fig. 2, which suggest that the Pa β profile is usually narrower than the H₂ and [Fe II] profiles. In Figure 6 we over-plot the Pa β , [Fe II] and H₂ line profiles from each CNSFR, which suggests that indeed the H₂ and [Fe II] profiles are broader than that of Pa β for most regions, although it should be noticed that the Pa β is only marginally resolved in our spectra.

4 DISCUSSION

4.1 Origin of the H₂ and [Fe II] emission from the ring of CNSFRs

The [Fe II] λ 1.25 μm /Pa β line ratio can be used to investigate the excitation mechanism of the [Fe II] emission. Some studies indicate that the [Fe II] emission in active galaxies can be produced by shocks due to the interaction of radio jets with the interstellar medium (Forbes & Ward 1993; Dopita & Sutherland 1996), while other studies indicate that photo-ionization can produce most of the observed [Fe II] emission (Simpson et al. 1996; Dors et al. 2012). A way to disentangle what are the main excitation mechanisms of the [Fe II] emission is based on the use of [Fe II] λ 1.25 μm /Pa β flux ratio (Reunanen, Kotilainen & Prieto 2002; Rodríguez-Ardila et al. 2004; Rodríguez-Ardila, Riffel & Pastoriza 2005; Riffel et al. 2013; Colina et al. 2015). Typical values for Seyfert nuclei are $0.6 < [\text{Fe II}]1.2570 \mu\text{m}/\text{Pa}\beta < 2.0$, while smaller values than 0.6 are observed for Starburst galaxies and H II regions and values higher than 2.0 may be associated to shocks, e.g. due to radio jets or supernovae explosions (e.g. Rodríguez-Ardila et al. 2004). As observed in the left panel of Fig. 5, the [Fe II] λ 1.25 μm /Pa β flux ratio map presents values smaller than 2.0 at all locations of the ring

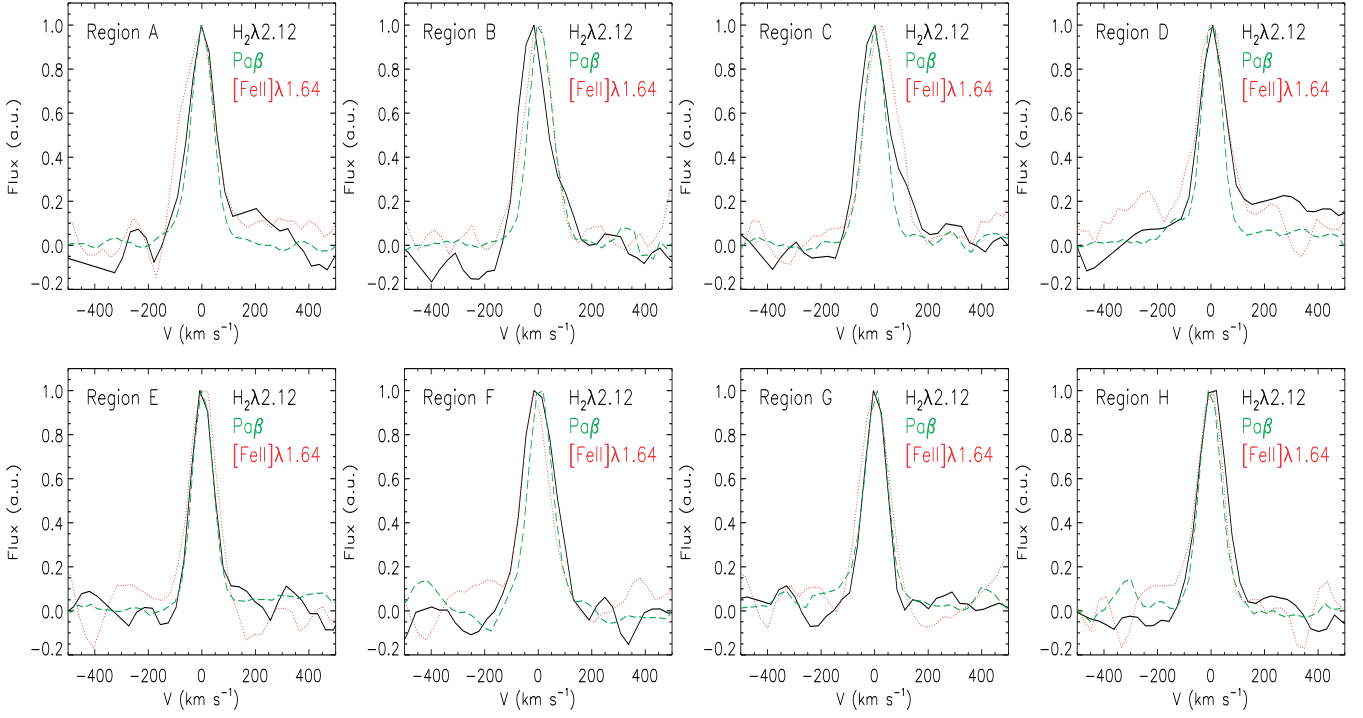


Figure 6. Emission-line profiles of $\text{H}_2\lambda 2.12\mu\text{m}$ (black), $\text{Pa}\beta$ (green) and $[\text{FeII}]\lambda 1.64\mu\text{m}$ (red) for the CNSFRs. The panels show the normalized flux vs. velocity in units of km s^{-1} for each CNSFR.

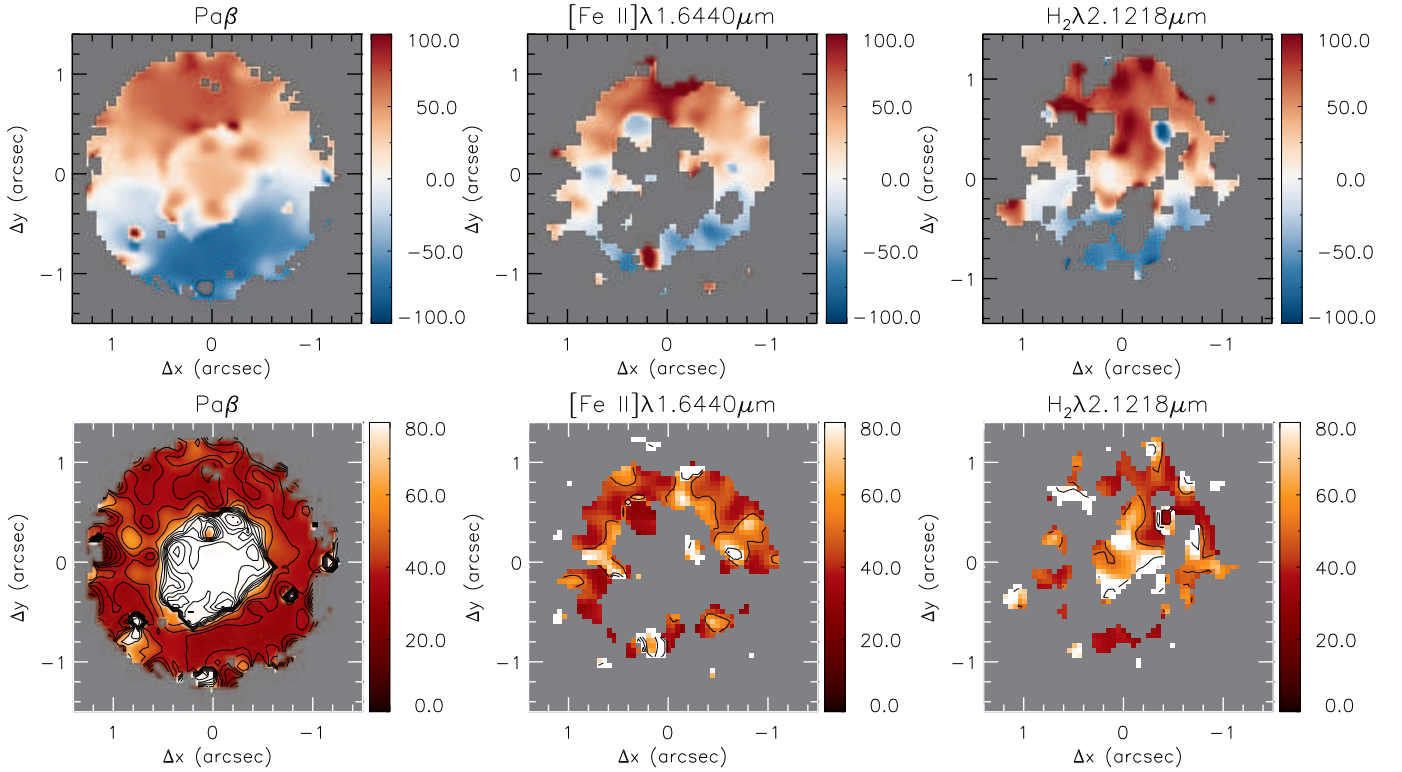


Figure 7. Gas velocity fields (top) and velocity dispersion σ maps (bottom) for the $\text{Pa}\beta$ (left), $[\text{FeII}]\lambda 1.64\mu\text{m}$ (center) and $\text{H}_2\lambda 2.12\mu\text{m}$ (right) emission lines. The color bars are shown in units of km s^{-1} .

of CNSFRs, indicating that the origin of the [Fe II] line emission is photo-ionization by young stars.

The origin of the H₂ emission in active galaxies has been addressed by several studies (e.g. Reunanen, Kotilainen & Prieto 2002; Rodríguez-Ardila et al. 2004; Rodríguez-Ardila, Riffel & Pastoriza 2005; Davies et al. 2005; Ramos Almeida, Pérez García & Acosta-Pulido 2009; Riffel et al. 2006, 2010, 2013; Dors et al. 2012; Colina et al. 2015). In summary, the H₂ lines can be originated by two mechanisms: (i) fluorescent excitation through absorption of soft-UV photons, e.g. from H II regions or AGNs (Black & van Dishoeck 1987) and (ii) collisional excitation due to heating of the gas by shocks (Hollenbach & McKee 1989) or by X-rays from the AGN (Maloney, Hollenbach & Tielens 1996). The H₂ λ 2.12 μm/Brγ line ratio can be used to investigate the H₂ main excitation mechanism: values smaller than 0.6 are commonly observed in H II regions and Starburst galaxies, where the H₂ lines are originated by fluorescence, while larger values are observed for AGNs and supernova remnants, where heating of the gas by X-rays and shocks may dominate (e.g. Rodríguez-Ardila, Riffel & Pastoriza 2005; Dors et al. 2012; Riffel et al. 2013; Colina et al. 2015). For Mrk 42, the H₂ λ 2.12 μm/Brγ flux ratio map (middle panel of Fig. 5) show values smaller than 0.6 at all locations of the CNSFRs ring, indicating that the observed H₂ emission is produced by fluorescent excitation due to absorptions of UV photons emitted by young stars.

4.2 A nuclear Starburst in Mrk 42

Using the flux values presented in Table 1 for the nucleus of Mrk 42 we obtain very low H₂ λ 2.12 μm/Brγ and [Fe II] λ 1.25 μm/Paβ values. Both ratios show values smaller than ~0.1, which are not consistent with those usually observed for Seyfert nuclei (larger than 0.6 for both ratios, Rodríguez-Ardila et al. 2004).

By fitting the SDSS (Albareti et al. 2017; Blanton et al. 2017) spectrum of Mrk 42, we obtain [N II] λ 6583/Hα ≈ 0.2 and [O III] λ 5007/Hβ ≈ 3, which put the nucleus of Mrk 42 in the Starburst region of the BPT diagram (Baldwin, Phillips & Terlevich 1981), consistent near-IR line ratios, although it should be noticed that the SDSS spectrum is obtained for an aperture of 3'' diameter, which includes the CNSFRs ring. However, it is well known that this galaxy presents an type 1 AGN, as broad recombination lines are detected. The low-emission line ratios detected at optical and near-IR can be explained if, besides the central AGN, Mrk 42 presents also strong nuclear Starburst activity, which dominates the gas excitation. Similar nuclear Starbursts are seen in other galaxies with CNSFRs rings, as for NGC 4303 (Colina & Arribas 1999; Colina et al. 2002; Riffel et al. 2016).

4.3 Gas kinematics

The velocity fields presented in Fig. 7 clearly show a rotation component. In order to obtain the kinematical and geometrical parameters, we have fitted the observed Paβ velocities by a rotating disk model, assuming circular orbits in the plane

of the galaxy, using the following equation (Bertola et al. 1991):

$$V_r(R, \Psi) = V_s + \frac{AR \cos(\Psi - \Psi_0) \sin(i) \cos^p \theta}{R^2 [\sin^2(\Psi - \Psi_0) + \cos^2(i) \cos^2(\Psi - \Psi_0)] + c_0^2 \cos^2(i)^{p/2}}, \quad (2)$$

where V_r is the circular velocity and R and Ψ are the coordinates of each pixel in the plane of the sky, V_s is the systemic velocity, A is the amplitude of the rotation curve in the plane of the galaxy, Ψ_0 is the position angle of the line of nodes, c_0 is a concentration parameter, defined as the radius where the rotation curve reaches 70% of the velocity amplitude, i is the disc inclination relative to the plane of the sky and p is a model fitting parameter. The parameter p measures the slope of the rotation curve where it flattens, in the outer region of the galaxy and it is limited between $1 \leq p \leq 3/2$. For $p=1$ the rotation curve at large radii is asymptotically flat while for $p=3/2$ the system has a finite mass.

We fitted the Paβ velocity field by the equation above using the MPFITFUN routine (Markwardt et al. 2009) to perform a non-linear least-squares fit, where initial guesses are given for each parameter and the routine returns their values for the best fitted model. The Paβ velocity field was chosen because the Paβ emission line presents the highest signal-to-noise ratio among the observed emission lines. During the fit, we excluded regions at $r < 0''.45$ from the nucleus, where an additional kinematic component is observed. During the fit, the position of the kinematical center was kept fixed at the nucleus, defined as the location of the peak of the continuum emission.

The resulting kinematical model is shown in the middle panel of Fig. 9, while the observed Paβ velocity field is shown in the left panel. Gray locations represent masked positions, where we were not able to obtain good velocity measurements (distances larger than 1'' from the nucleus) and the nuclear region, where outflows from the central AGN seem to co-exist with a disk component. The residual map, obtained as the difference between the observed velocities and the model is presented in the right panel. The residual map presents values very close to zero at all locations (smaller than 10 km s⁻¹), showing that the velocity field is well represented by the model and thus, dominated by regular rotation.

The resulting parameters for the best fit model are: $i = 20.2^\circ \pm 2.0^\circ$, $V_s = 7391 \pm 11$ km s⁻¹, corrected to the heliocentric reference frame, $A = 259 \pm 24$ km s⁻¹, $\Psi_0 = 8^\circ \pm 1^\circ$, $c_0 = 0.56 \pm 0.05$ arcsec and $p = 1.5$, which was limited between 1 and 1.5. The disk inclination is slightly larger than that of the large scale disk, obtained assuming $i = \arccos(b/a)$, where a and b are the semi-major and semi-minor axis of the galaxy and the value of the systemic velocity ($V_s = 7385$ km s⁻¹) is in a good agreement with that of Falco et al. (1999). The orientation of the line of nodes is similar to that of the large scale disk, quoted in the Hyperleđa database ($\Psi_0 = -12^\circ$, Makarov et al. 2014).

Within the inner $r < 0''.45$ radius, the Paβ emission line seems to present two narrow kinematic components: the blueshifted component is seen with velocity of $V_{\text{blue}} \approx -300$ km s⁻¹, relative to the systemic velocity, while the redshifted component is seen with velocities very close to the nuclear velocity. The blueshifted component is only marginally

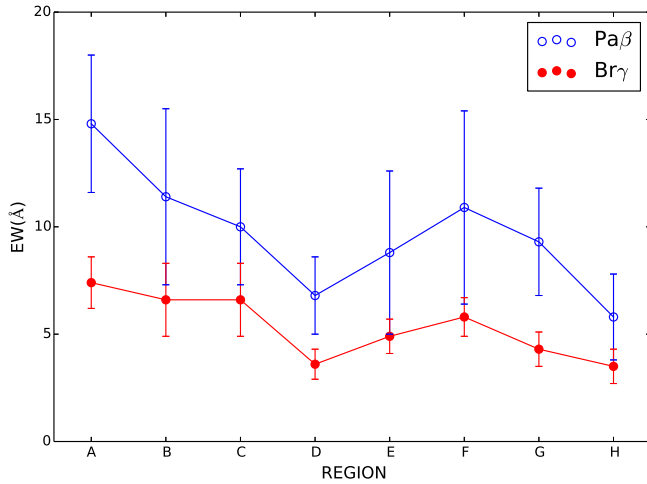


Figure 8. Sequence of values for the EqW of Pa β (open blue circles) and Br γ (filled red circles) emission lines for the CNSFRs labeled from ‘A’ to ‘H’ in Fig. 4.

detected and thus, we were not able to properly fit it. A possible interpretation of these two components is that the blueshifted one is originated from outflowing gas from the nucleus excited by the central AGN, while the redshifted one may be originated from the nuclear Starburst located at the disk of the galaxy.

4.4 Stellar populations and CNSFRs

We used the integrated emission-line fluxes of Table 1 to calculate the following properties: the mass of ionized M_{HII} gas; rate of ionizing photons $Q[\text{H}^+]$; the star formation rate (SFR) and the mass of hot molecular M_{H_2} .

The mass of ionized gas can be estimated by (e.g. Riffel et al. 2016)

$$\left(\frac{M_{\text{HII}}}{M_{\odot}}\right) = 3 \times 10^{19} \left(\frac{F_{\text{Br}\gamma}}{\text{erg cm}^{-2} \text{s}^{-1}}\right) \left(\frac{D}{\text{Mpc}}\right)^2 \left(\frac{N_e}{\text{cm}^{-3}}\right)^{-1}, \quad (3)$$

where $F_{\text{Br}\gamma}$ is the Br γ flux, D is the distance to the galaxy and N_e is the electron density, under the assumption of case B recombination at an electron temperature of 10^4K (Osterbrock & Ferland 2006). The mass of hot molecular gas can be estimated by (Scoville et al. 1982; Riffel et al. 2008)

$$\left(\frac{M_{\text{H}_2}}{M_{\odot}}\right) = 5.0776 \times 10^{13} \left(\frac{F_{\text{H}_2\lambda 2.1218}}{\text{erg cm}^{-2} \text{s}^{-1}}\right) \left(\frac{D}{\text{Mpc}}\right)^2, \quad (4)$$

where $F_{\text{H}_2\lambda 2.1218}$ is the flux of the $\text{H}_2 \lambda 2.1218$ emission line and we assume local thermal equilibrium and an excitation temperature of 2000 K for the H_2 .

The emission rate of ionizing photons is obtained following Riffel et al. (2009):

$$\left(\frac{Q[\text{H}^+]}{\text{s}^{-1}}\right) = 7.47 \times 10^{13} \left(\frac{L_{\text{Br}\gamma}}{\text{erg s}^{-1}}\right), \quad (5)$$

where $L_{\text{Br}\gamma}$ is the Br γ luminosity and the star formation rate is obtained by:

$$\left(\frac{SFR}{M_{\odot} \text{yr}^{-1}}\right) = 8.2 \times 10^{-40} \left(\frac{L_{\text{Br}\gamma}}{\text{erg s}^{-1}}\right), \quad (6)$$

following Kennicutt (1998). The equations above for SFR and $Q[\text{H}^+]$ are derived under the assumption of continuous star formation, and should be considered just proxies of these parameters.

In order to estimate the mass of ionized gas and the resulting physical properties of each CNSFR of Mrk 42 that are shown in Table 3, we have assumed the electron density value of $N_e = 300 \text{ cm}^{-3}$, which is the mean value of the electron density for a sample of CNSFRs derived from the $[\text{S II}]\lambda 6717/\lambda 6731$ intensity ratio by Díaz et al. (2007) and Dors et al. (2008).

The derived physical parameters for the CNSFRs of Mrk 42 can be compared with previously published values. Dors et al. (2008) used optical IFS to study the CNSFRs of the Seyfert 2 galaxies NGC 1097 and NGC 6951 and found SFR in the range $0.002\text{--}0.14 M_{\odot} \text{yr}^{-1}$ for the eight star-forming regions studied. Shi, Gu & Peng (2006) used the observations from the Sloan Digital Sky Survey (SDSS) to study a sample of 385 objects classified as star-forming galaxies and found an average value for the SFR of $0.14 M_{\odot} \text{yr}^{-1}$. Falcón-Barroso et al. (2014) used SINFONI data to study the star formation in the inner 700 pc of the active spiral galaxy NGC 613 and obtained $SFR \sim 10^{-2} - 10^{-1} M_{\odot} \text{yr}^{-1}$ for eight CNSFRs. Riffel et al. (2016) found SFR of $(0.4\text{--}2.0) \times 10^{-2} M_{\odot} \text{yr}^{-1}$ for the CNSFRs of NGC 4303 derived from SINFONI observations. Thus, the values of SFR derived for the ring of Mrk 42 ($0.07\text{--}0.2 M_{\odot} \text{yr}^{-1}$) are within the range of values observed for other galaxies with similar nuclear rings.

The emission rates of ionizing photons for the CNSFRs of Mrk 42 are in the range $\log(Q) = 51.8 - 52.3 \text{ photons s}^{-1}$, in agreement with values already obtained for CNSFRs in other galaxies (e.g. Galliano & Alloin 2008; Riffel et al. 2009; Wold & Galliano 2006; Riffel et al. 2016). Such rates correspond to more than hundred O3 stars in each CNSFR (Osterbrock & Ferland 2006), but these values should be considered only as a proxy as a continuous star formation regime was assumed and the most probable scenario may be that of instantaneous star formation.

Finally, the masses of ionized and hot molecular gas observed for Mrk 42 are similar to that observed for other CNSFRs (e.g. Riffel et al. 2016, 2009). The average ratio between the ionized and hot molecular gas masses is $<M_{\text{HII}}/M_{\text{H}_2}> \sim 3312$, being similar to that observed for the CNSFRs of NGC 4303 (2030, Riffel et al. 2016), and also in the range of values obtained for the inner kiloparsec of nearby Seyfert galaxies, of 200–8000 (e.g. Schönell et al. 2017; Riffel et al. 2018).

The total mass of ionized gas in the ring (derived by measuring the fluxes of Br γ and $\text{H}_2\lambda 2.12\mu\text{m}$ from an integrated spectrum comprising distances between $0''.45$ and $1''.3$ from the nucleus) is 1.9 times larger than the sum of M_{HII} of all CNSFRs. The total mass of hot molecular gas in the ring is 2.8 times larger than that of the CNSFRs, indicating that a large amount of gas is observed outside the CNSFRs.

We can also use the spectra shown in Fig. 2 to better

Table 3. Physical parameters of the CNSFRs in Mrk 42 from integrated emission-line fluxes shown in Table 1. The location of each region is indicated in Fig. 4. $Q[\text{H}^+]$ is the ionizing photons rate, SFR the star formation rate, M_{HII} is the mass of ionized gas and M_{H2} the mass of hot molecular gas.

Region	$\log Q[\text{H}^+] \text{ (s}^{-1}\text{)}$	SFR ($10^{-2}M_{\odot}\text{yr}^{-1}$)	$M_{\text{HII}} \text{ (}10^4M_{\odot}\text{)}$	$M_{\text{H2}} \text{ (}M_{\odot}\text{)}$
A	52.3 ± 0.06	21.5 ± 3.30	21.9 ± 3.36	43.0 ± 9.20
B	51.8 ± 0.06	7.4 ± 1.20	7.6 ± 1.23	23.6 ± 6.65
C	51.8 ± 0.06	7.4 ± 1.17	7.5 ± 1.19	23.6 ± 5.30
D	51.8 ± 0.07	7.6 ± 1.43	7.7 ± 1.46	23.0 ± 4.72
E	51.9 ± 0.05	8.2 ± 0.93	8.4 ± 0.95	17.9 ± 3.67
F	51.8 ± 0.05	7.8 ± 0.94	7.9 ± 0.96	38.5 ± 7.86
G	51.8 ± 0.05	6.9 ± 0.89	7.0 ± 0.91	25.7 ± 4.25
H	51.8 ± 0.08	6.4 ± 1.27	6.5 ± 1.30	29.6 ± 4.13
Ring	53.1 ± 0.04	138.7 ± 12.89	141.43 ± 13.13	624.3 ± 87.19

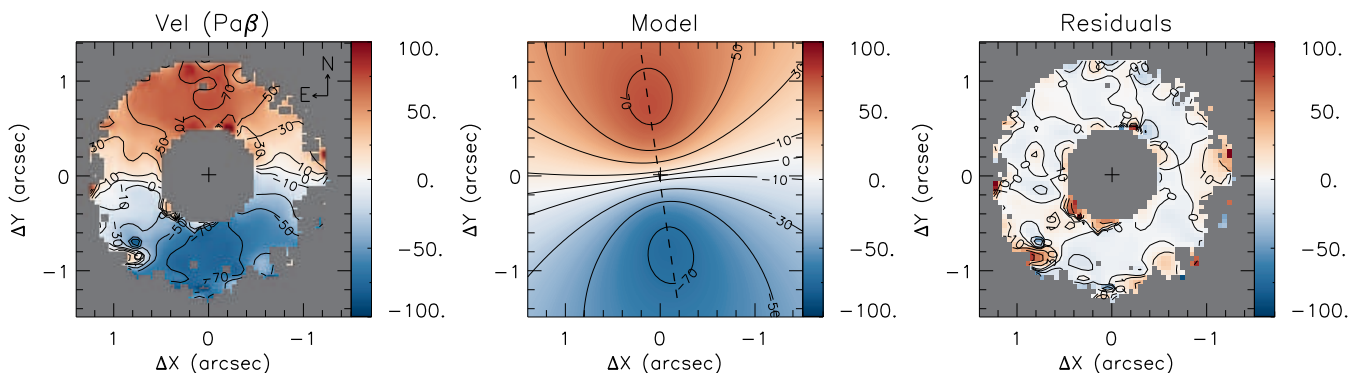


Figure 9. Left panel: $\text{Pa}\beta$ velocity field; middle: rotating disk model and right: residual map, obtained as the difference of the observed velocities and the model. The color bars show the velocity in units of km s^{-1} and the central cross indicates the position of the nucleus. The external gray regions represent masked locations where the signal-to-noise ratio of $\text{Pa}\beta$ was not high enough to allow a good fit of its profile, while the gray region at $r < 0''.45$ represents masked locations, where gas outflows are suggested. The central cross marks the position of the nucleus.

investigate the stellar content of the CNSFRs. These spectra show strong absorption features at $1.17\text{--}1.20 \mu\text{m}$, which may be molecular absorptions from stars in the thermally pulsing asymptotic giant branch (TP-AGB) phase, as suggested by simple stellar populations models (Maraston 2005) and detected in the nuclear spectra of nearby AGNs (e.g. VO and CN features, Riffel et al. 2007, 2015). In addition, these features are clearly present in the spectra of stars in the TP-AGB phase (Maraston 2005; Rayner et al. 2009). By comparing the spectra of the CNSFRs ‘E’, ‘F’ and ‘G’, with the stellar spectra shown by ?, one can see that similar features are also seen in the spectra of oxygen (e.g. from TiO and VO) and carbon (e.g. CN features) rich stars in the upper AGB phase. Martins et al. (2013a) also reported the detection of signatures of stellar population dominated by the TP-AGB (as CN, TiO and ZrO absorptions) in near-IR spectra of H II galaxies, which show a similar absorption features at $\sim 1.19 \mu\text{m}$ as seen in the CNSFRs of Mrk 42. However, stellar population synthesis performed for star-forming galaxies by Martins et al. (2013b) do not find a clear correlation between the near-IR (e.g. CN) indexes and the presence of intermediate-age stellar populations, but this is attributed by these authors as due to observational limitations. Thus, the detection of these molecular features in the CNSFRs ‘E’, ‘F’ and ‘G’ suggests that these regions are older than the

other CNSFRs of Mrk 42 and already present some evolved stars.

4.5 How does the star formation proceed in the CNSFRs ring?

Gas inflows towards the central region of galaxies provide a gas reservoir, which can trigger (circum-)nuclear star formation and a central AGN. The way the material flows towards the central region may be through bars, spiral arms or interactions with neighbor galaxies. Inflows of gas associated to nuclear dust spirals and bars have been observed for nearby active galaxies at scales of a few hundred parsecs, mostly using optical and near-IR IFS (e.g. Riffel et al. 2008; Fathi et al. 2006; Storchi-Bergmann et al. 2007; Müller Sánchez et al. 2009; van de Ven & Fathi 2010; Riffel, Storchi-Bergmann & Winge 2013; Schnorr-Müller et al. 2014a; Schnorr-Müller et al. 2017), but the presence of nuclear dust structures is not a sufficient condition to produce gas streaming (Brum et al. 2017).

Two possible scenarios have been proposed for the origin of the CNSFRs at scales of few hundred parsecs: the *popcorn* and *pearls on a string* scenarios (Böker et al. 2008) that show distinct distributions in age of the stellar clusters. In the *popcorn* scenario, the gas is accumulated in the

circumnuclear region resulting in a ring of higher density material, which allows a simultaneous star formation in the whole ring or in individual hotspots, collapsing at different times within the ring. Thus, for this scenario there is no relation between the age of the recent formed stellar clusters and their locations within the ring.

In the *pearls on a string* scenario, a short-lived, quasi-instantaneous burst of star formation is induced and located in a certain region of the ring. The locations of these over-density regions (ODR, where the gas density is high enough to trigger the star formation) depends on details of the gravitational potential, but they are frequently found at locations where the gas reaches the central region, as for example, at the tips of bars. Stellar clusters are formed in these ODRs, which follow orbits within the ring, resulting in several stellar clusters with a sequence of ages, and are called “pearls on a string”. Thus, in this scenario, two segments of stellar clusters, on opposite sides of the ring, are expected in which the youngest clusters have their locations near the ODRs, becoming older when approaching the opposite ODR, i.e. there is a correlation between the stellar cluster age and the ring localization.

In order to distinguish between the *popcorn* and *pearls on a string* scenarios for the origin of the ring of CNSFRs in Mrk 42, we constructed Fig. 8 that shows the sequence of EqW values for Pa β (open blue circles) and Br γ (filled red circles) emission lines for the regions labeled from ‘A’ to ‘H’. The EqW values were measured from the integrated spectra of Fig. 2 and are shown in Table 2. The EqW values of H recombination lines can be used to determine the age of the star formation regions, with higher values observed for younger regions and lower values for older regions, under the assumption that all regions are intrinsically equal in stellar mass and the mass in the burst is the same (Dottori 1981; Copetti et al. 1986). By comparing Br γ EqW values observed for the CNSFRs of Mrk 42 with the predicted values by evolutionary photo-ionization models (Riffel et al. 2009; Dors et al. 2008), we conclude that all regions have ages between 5 and 6 Myr, considering the correction due to the contribution to the bulge stars to the underlying continuum in the derived EqW values, as discussed in Sec. 3.1. The highest EqW values are observed for region ‘A’, decreasing to a minimum value for region ‘D’. A second gradient is seen from region ‘F’ to ‘H’. As the EqW of the H recombination lines can be associated with the age of the stars, these gradients can be interpreted as a signature of two age sequences, one from region ‘A’ to ‘D’ and another from region ‘F’ to ‘H’, favoring thus the *pearls on a string* scenario if the gas reaches the center along the major axis of the galaxy (close to the orientation of the bar - see Fig. 4). On the other hand, the spectra for the regions ‘E’, ‘F’ and ‘G’ clearly show the presence of the molecular absorption bands at 1.17–1.20 μm . These absorptions (TiO, CN or VO) are originated in more evolved stars that are in the TP-AGB phase (e.g. Maraston 2005; ?), indicating that these regions are older than the remaining and suggests no clear sequence in age for these CNSFRs and thus not supporting the above sequence of ages for these CNSFRs.

4.6 Mass of the SMBH

The mass of the SMBH can be obtained directly from the Pa β width and luminosity using the following equation (Kim et al. 2015, 2010; Woo et al. 2015):

$$\frac{M_{\text{BH}}}{M_{\odot}} = 10^{7.04 \pm 0.02} \left(\frac{L_{\text{Pa}\beta}}{10^{42} \text{ergs}^{-1}} \right)^{0.48 \pm 0.03} \left(\frac{\text{FWHM}_{\text{Pa}\beta}}{10^3 \text{kms}^{-1}} \right)^2, \quad (7)$$

where $L_{\text{Pa}\beta}$ is the luminosity and $\text{FWHM}_{\text{Pa}\beta}$ corresponds to width of the broad Pa β component. Assuming $L_{\text{Pa}\beta} = (9.0 \pm 0.3) \times 10^{39} \text{ergs}^{-1}$ and $\text{FWHM}_{\text{Pa}\beta} = 1480 \pm 40 \text{kms}^{-1}$, measured from the Pa β profile within a circular aperture of 0''25 radius, we obtain $M_{\text{BH}} = 2.5_{-0.6}^{+0.7} \times 10^6 M_{\odot}$.

The mass of the SMBH of Mrk 42 derived here is in good agreement with values obtained using scaling relations based on optical observations and based on the X-ray excess variance, which are in the range $(0.7\text{--}18) \times 10^6 M_{\odot}$ (Wang & Lu 2001; Bian & Zhao 2003; Nikolajuk, Czerny & Gurynowicz 2009).

We notice that the width of the Pa β broad emission line is larger by a factor of 1.7–2.2 than those quoted in the literature for the H β broad component (Goodrich 1989; Bian & Zhao 2003; Wang & Lu 2001). However, it should be noted that the values of FWHM for H β available in the literature are based on more than 20 years old low resolution spectra. Using the Sloan Digital Sky Survey (SDSS, Albareti et al. 2017; Blanton et al. 2017) spectrum of Mrk 42, we note that the broad H β component is just marginally detected, but its width is consistent with our measurement for Pa β . The H α broad component of Mrk 42 is clearly detected in the SDSS spectrum and has a $\text{FWHM} \approx 1400 \text{kms}^{-1}$, being similar to that derived for Pa β .

5 CONCLUSIONS

We used J, H and K bands Gemini NIFS observations to map the flux distributions and kinematics in the near-IR emission lines of the inner $1.5 \times 1.5 \text{kpc}^2$ of Mrk 42 at a spatial resolution of 60 pc and velocity resolution of $\sim 40 \text{kms}^{-1}$. The main conclusions of this work are:

- The emission-line flux distributions and EqW maps clearly show the ring of CNSFRs, previously detected in HST image at $\sim 300 \text{pc}$ from the nucleus. We detected 8 CNSFRs (labeled from ‘A’ to ‘H’) in the ring and by comparing the observed EqW values of the Br γ emission line with those predicted by photo-ionization models, we conclude that their age is between 5 and 6 Myr. These regions present star formation rates in the range 0.06–0.21 $M_{\odot} \text{yr}^{-1}$, ionizing photons rate of $\log(Q) = 51.8 - 52.3$ photons s^{-1} , masses of ionized gas in the range $(6.5\text{--}22) \times 10^4 M_{\odot}$ and masses of hot molecular gas between 18 and 43 M_{\odot} . These masses represent $\approx 53\%$ and 36% of the total masses in the ring, respectively.
- In addition to a central AGN, line-intensity ratios indicate that Mrk 42 harbors a nuclear Starburst.
- The spectra of the regions ‘E’, ‘F’ and ‘G’ show molecular absorption bands at 1.17–1.20 μm , possibly originated from evolved stars at the TP-AGB phase.
- The near-IR emission lines of [Fe II] and H $_2$ from the

star forming regions have as main ionizing source young stars with 5–6 Myr of age.

- The gas velocities at locations beyond the inner 0''45 (~ 220 pc) are dominated by rotation, being well reproduced by a disk model assuming circular orbits in the plane of the galaxy. At the nucleus, the gas kinematics suggests two components: one due to the disk of the galaxy, with V_{LOS} similar to the systemic velocity of the galaxy ($7391 \pm 11 \text{ km s}^{-1}$) and another blueshifted by 300–500 km s^{-1} , attributed to a nuclear outflow.

- The EqW values of the Br γ emission line suggest two age sequences, one from region ‘A’ to ‘D’ and another from region ‘F’ to ‘G’. These age sequences favor the ‘pearls on a string’ scenario for the origin of the CNSFRs in Mrk 42, although the presence of signatures of TP-AGB stars in some of the regions undermines this interpretation.

- The FWHM of the broad component of Pa β emission line is $\sim 1480 \text{ km s}^{-1}$, being larger than the values previously observed for H β . Using this value we obtain a mass of $M_{\text{BH}} = 2.5_{-0.6}^{+0.7} \times 10^6 M_{\odot}$ for the central supermassive black hole.

ACKNOWLEDGEMENTS

We thank the anonymous referee for valuable suggestions which helped to improve the paper. This work is based on observations obtained at the Gemini Observatory, which is operated by the Association of Universities for Research in Astronomy, Inc., under a cooperative agreement with the NSF on behalf of the Gemini partnership: the National Science Foundation (United States), the Science and Technology Facilities Council (United Kingdom), the National Research Council (Canada), CONICYT (Chile), the Australian Research Council (Australia), Ministério da Ciência e Tecnologia (Brazil) and south-east CYT (Argentina). This research has made use of the NASA/IPAC Extragalactic Database (NED) which is operated by the Jet Propulsion Laboratory, California Institute of Technology, under contract with the National Aeronautics and Space Administration. We acknowledge the usage of the HyperLeda database (<http://leda.univ-lyon1.fr>). The authors acknowledge support from CNPq and FAPERGS. O.L.D. is grateful to FAPESP (2016/04728-7) and CNPQ (306744/2014-7).

REFERENCES

- Albaret, F. D et al., 2017, ApJS, 233, 25.
 Baldwin, J. A., Phillips, M. M., Terlevich, R., 1981, PASP, 93, 5
 Bertola, F., Bettoni, D., Danziger, J., et al. 1991, ApJ, 373, 369.
 Bian W., Zhao Y., 2003, MNRAS, 343, 164.
 Black, J. H., & van Dishoeck, E. F. 1987, ApJ, 322, 412.
 Blanton, M. R. et al., 2017, AJ, 154, 28.
 Böker, T., Falcón-Barroso, J., Schinnerer, E., Knapen, J. H., & Ryder, S. 2008, AJ, 135, 479.
 Brum, C., Riffel, R. A., Storchi-Bergmann, T., Robinson, A., Schnorr-Muller, A., Lena, D., 2017, MNRAS, accepted.
 Cardelli, J. A., Clayton, G. C. & Mathis, J. S., 1989, ApJ, 345, 245.
 Colina, L., Arribas, S., 1999, ApJ, 514, 637.
 Colina, L., Gonzalez Delgado, R., Mas-Hesse, J. M., & Leitherer, C. 2002, ApJ, 579, 545.
 Colina L., Piqueras-Lopez J., Arribas S., R. Riffel, Rodriguez-Ardila, Pastoriza, M. G., Storchi-Bergmann T., Alonso-Herrero & Sales D., 2015, A&A, 578, 48.
 Copetti, M. V. F., Pastoriza, M. G., & Dottori, H. A. 1986, A&A, 156, 111.
 Davies, R. I., I., Sternberg, A., Lehnert, M. D., & Tacconi-Garman, L. E., 2005, ApJ, 633, 105.
 Davies, R. I., Müller Sánchez, F., Genzel, R., et al., 2007, ApJ, 671, 1388.
 Deo, R. P.; Crenshaw, D. M.; Kraemer, S. B., 2006, AJ, 132, 321.
 Díaz, Á. I., Terlevich, E., Castellanos, M., & Hägele, G. F. 2007, MNRAS, 382, 251.
 Diniz, M. R., Riffel, R. A., Storchi-Bergmann, T., Winge, C., 2015, MNRAS, 453, 1727.
 Dottori, H. A. 1981, Ap&SS, 80, 267.
 Dopita, M. A., & Sutherland, R. S., 1996, ApJS, 102, 161
 Dors, O. L., Jr., Storchi-Bergmann, T., Riffel, R. A., & Schimdt, A. A., 2008, A&A, 482, 59.
 Dors, O. L., Jr., Riffel, R. A., Cardaci, M. V., et al., 2012, MNRAS, 422, 252.
 Elmegreen, B. G. 1994, ApJL, 425, L73.
 Falco, E. E., Kurtz, M. J., Geller, M. J., et al., 1999, PASP, 111, 438.
 Falcón-Barroso, J., Ramos Almeida, C., Böker, T., et al. 2014, MNRAS, 438, 329.
 Fathi, K., Storchi-Bergmann, T., Riffel, R. A., Winge, C., Axon, D. J., Robinson, A., Capetti, A., & Marconi, A., 2006, ApJL, 641, L25.
 Ferrarese, L., & Merritt, D. 2000, ApJL, 539, L9.
 Forbes, D. A. & Ward, M. J. 1993, ApJ, 416, 150.
 Galliano, E., & Alloin, D. 2008, A&A, 487, 519.
 Gebhardt, K., Bender, R., Bower, G., et al. 2000, ApJL, 539, L13.
 Goodrich, R.W. 1989, ApJ 342, 224
 Hollenbach, D., & McKee, C. F., 1989, ApJ, 342, 306.
 Hunt, L. K., & Malkan, M. A., 1999, ApJ, 516, 660.
 Hunt, L. K., Malkan, M. A., Rush, B., Bica, M. D., Nelson, B. O., Stanga, R. M., Webb, W., 1999, ApJS, 125, 349.
 Joglee, S., Scoville, N., & Kenney, J. D. P. 2005, ApJ, 630, 837.
 Kennicutt, R. C., Keel, W., & Blaha, C. A. 1989, ApJ, 97, 1022
 Kennicutt, R. C., Jr., 1998, ARA&A, 36, 189.
 Kim, D., Im, M., & Kim, M. 2010, ApJ, 724, 386
 Kim, D., Im, M., Glikman, E., Woo, J.-H., & Urrutia, T. 2015, ApJ, 812, 66.
 Knapen, J. H., 2005, A&A, 429, 141.
 Kotilainen, J. K., Reunanen, J., Laine, S., & Ryder, S. D. 2000, A&A, 353, 834.
 Lançon, A., & Mouhcine, M., 2002, A&A, 393, 167.
 Lamperti, I. et al., 2017, MNRAS, 467, 540.
 Larkin, J. E., Armus, L., Knop, R. A., Soifer, B. T., Matthews, K., 1998, ApJS, 114, 59.
 Makarov, D., Prugniel, P., Terekhova, N., Courtois, H., Vauglin, I., 2014, A&A, 570, 13
 Malkan, M. A., Gorjian, V., & Tam, R. 1998, ApJS, 117, 25.
 Maloney, P. R., Hollenbach, D. J., & Tielens, A. G. G. M., 1996, ApJ, 466, 561.
 May, D., Steiner, J. E., Ricci, T. V., Menezes, R. B., Andrade, I. S., 2016, MNRAS, 457, 949.
 Maraston, C. 2005, MNRAS, 362, 799.
 Markwardt C. B., 2009, in Bohlender D. A., Durand D., Dowler P., eds, ASP Conf. Ser. Vol. 411, Astronomical Data Analysis Software and Systems XVIII. Astron. Soc. Pac., San Francisco, p. 251
 Martins, L. P., Rodríguez-Ardila, A., Diniz, S., Gruenwald, R., & de Souza, R. 2013, MNRAS, 431, 1823.
 Martins, L. P., Rodríguez-Ardila, A., Diniz, S., Riffel, R., & de Souza, R. 2013, MNRAS, 435, 2861.
 Mazzuca, L. M., Knapen, J. H., Veilleux, S., & Regan, M. W. 2008, ApJS, 174, 337-365.
 McGregor, P. J. et al., 2003, Proceedings of the SPIE, 4841, 1581.
 Morgan, W. W. 1958, PASP, 70, 364.
 Müller Sánchez, F., Davies, R. I., Genzel, R., Tacconi, L. J., Eisen-

- hauer, F., Hicks, E. K. S., Friedrich, S., Sternberg, A., 2009, *ApJ*, 691, 749.
- Muñoz Marín, V. M., González Delgado, R. M., Schmitt, H. R., et al. 2007, *AJ*, 134, 648.
- Nikolajuk, M., Czerny, B., Gurynowicz, P., 2009, *MNRAS*, 394, 2141.
- Norman, C., & Scoville, N. 1988, *ApJ*, 332, 124.
- Osterbrock, D. E. & Ferland, G. J., 2006, *Astrophysics of Gaseous Nebulae and Active Galactic Nuclei*, Second Edition, University Science Books, Mill Valley, California.
- Perry, J. J., & Dyson, J. E., 1985, *MNRAS*, 213, 665.
- Ramos Almeida, C., Pérez García, A. M., & Acosta-Pulido, J. A., 2009, *ApJ*, 694, 1379.
- Rayner, J. T., Cushing, M. C., & Vacca, W. D., 2009, *ApJS*, 185, 289.
- Reunanen, J., Kotilainen, J. K., & Prieto, M. A., 2002, *MNRAS*, 331, 154.
- Ricci, T. V.; Steiner, J. E.; Menezes, R. B., *MNRAS*, 440, 2419.
- Riffel, Rogemar A., Storchi-Bergmann, T., Winge, C., Barbosa, F. K. B., 2006, *MNRAS*, 373, 2.
- Riffel, Rogemar A., Storchi-Bergmann, T., Winge, C., McGregor, P. J., Beck, T., Schmitt, H. 2008, *MNRAS*, 385, 1129.
- Riffel, Rogemar A., Storchi-Bergmann, T., Dors, O. L., Winge, C., 2009, *MNRAS*, 393, 783.
- Riffel, Rogemar A., 2010, *Ap&SS*, 327, 239.
- Riffel, Rogemar A. & Storchi-Bergmann, T., 2011, *MNRAS*, 411, 469.
- Riffel, R. A., Storchi-Bergmann, T., Winge, C., 2013, 430, 2249.
- Riffel, Rogemar A., & Storchi-Bergmann, T. & Nagar, N. M., 2010, *MNRAS*, 404, 166.
- Riffel, Rogemar A., Colina, L., Storchi-Bergmann, T., Piqueras López J., Arribas, S., Riffel, R., Pastoriza, M., Sales, Dinalva A., Dametto, N. Z., Labiano, A. & Davies, R. I., 2016, *MNRAS*, 461, 4192.
- Riffel, R. A. et al., 2018, *MNRAS*, 474, 1373.
- Riffel, R., Pastoriza, M. G., Rodríguez-Ardila, A., Maraston, C., 2007, *ApJ*, 659, 103.
- Riffel, R., Bonatto, C., Cid Fernandes, R., Pastoriza, M. G., & Balbinot, E. 2011, *MNRAS*, 411, 1897.
- Riffel, R., Rodríguez-Ardila, A., Aleman, I., et al. 2013, *MNRAS*, 430, 2002.
- Riffel, R. et al., 2015, *MNRAS*, 450, 3069.
- Rodríguez-Ardila, A., Pastoriza, M. G., Viegas, S., Sigut, T. A. A., & Pradhan, A. K., 2004, *A&A*, 425, 457.
- Rodríguez-Ardila, A., Riffel, R., & Pastoriza, M. G. 2005, *MNRAS*, 364, 1041.
- Sakamoto, K., Okumura, S. K., Ishizuki, S., & Scoville, N. Z. 1999, *ApJ*, 525, 691.
- Sani, E., Lutz, D., Risaliti, G., Netzer, H., Gallo, L. C., Trakhtenbrot, B., Sturm, E., Boller, T., 2010, *MNRAS*, 403, 1246.
- Schönnell, A. J., Riffel, R. A., Storchi-Bergmann, T., & Riffel, R. 2017, *MNRAS*, 464, 1771.
- Schnorr-Müller, Allan; Storchi-Bergmann, T., Nagar, N. M., Lena, D., Riffel, R. A., Couto, G. S., 2014b, 2014a, *MNRAS*, 438, 3322.
- Schnorr-Müller, Allan; Storchi-Bergmann, T., Nagar, N. M., Robinson, A., Ferrari, F., *MNRAS*, 437, 1708.
- Schnorr Müller A., Storchi-Bergmann T., Ferrari, F., Nagar, N. M., 2017, *MNRAS*, 466, 4370.
- Schwarz, M. P. 1981, *ApJ*, 247, 77
- Scoville, N. Z., Hall, D. N. B., Ridgway, S. T., & Keinmann, S. G. 1982, *ApJ*, 253, 136.
- Sérsic, J. L., & Pastoriza, M. 1967, *PASP*, 79, 152.
- Shi, L., Gu, Q. S., & Peng, Z. X. 2006, *A&A*, 450, 15.
- Simões Lopes R. D., Storchi-Bergmann T., de Fátima Saraiva M. & Martini P., 2007, *ApJ*, 655, 718.
- Simpson, C., Forbes, D. A., Baker, A. C., & Ward, M. J. 1996, *MNRAS*, 283, 777.
- Storchi-Bergmann, T., Dors Jr., O., Riffel, R. A., Fathi, K., Axon, D. J., & Robinson, A., 2007, *ApJ*, x, x.
- Storchi-Bergmann, T. 2008, *Revista Mexicana de Astronomia y Astrofisica Conference Series*, 32, 139.
- van de Ven, G., & Fathi, K., 2010, *ApJ*, 723, 767.
- van der Laan, T. P. R., Armus, L., Beirao, P., et al. 2015, *A&A*, 575, A83.
- Wang T., Lu Y., 2001, *A&A*, 377, 52.
- Wilson, A. S., Helfer, T. T., Haniff, C. A., & Ward, M. J., 1991, *ApJ*, 381, 79.
- Wold, M., Galliano, E., 2006, *MNRAS*, 369, 47.
- Woo, J.-H., Yoon, Y., Park, S., Park, D., & Kim, S. C. 2015, *ApJ*, 801, 38